RSC Advances

PAPER

View Article Online
View Journal | View Issue

Cite this: *RSC Adv.*, 2018, **8**, 24110

Formamidinium-based planar heterojunction perovskite solar cells with alkali carbonate-doped zinc oxide layer†

Jaeki Jeong,‡[a] Haeyeon Kim,‡[a] Yung Jin Yoon,[a] Bright Walker,[c] Seyeong Song,[a] Jungwoo Heo,[b] Song Yi Park,[a] Jae Won Kim,[a] Gi-Hwan Kim*[a] and Jin Young Kim *[a]

Received 27th March 2018
Accepted 8th June 2018

DOI: 10.1039/c8ra02637h

rsc.li/rsc-advances

We herein demonstrate n-i-p-type planar heterojunction perovskite solar cells employing spin-coated ZnO nanoparticles modified with various alkali metal carbonates including Li_2CO_3, Na_2CO_3, K_2CO_3 and Cs_2CO_3, which can tune the energy band structure of ZnO ETLs. Since these metal carbonates doped on ZnO ETLs lead to deeper conduction bands in the ZnO ETLs, electrons are easily transported from the perovskite active layer to the cathode electrode. The power conversion efficiency of about 27% is improved due to the incorporation of alkali carbonates in ETLs. As alternatives to TiO_2 and n-type metal oxides, electron transport materials consisting of doped ZnO nanoparticles are viable ETLs for efficient n-i-p planar heterojunction solar cells, and they can be used on flexible substrates *via* roll-to-roll processing.

1. Introduction

Considerable efforts to develop renewable energy sources have been made in the last several decades, leading to the demonstration of several new classes of highly efficient photovoltaic cells. Inorganic, organic and hybrid light absorbers such as organic bulk heterojunctions, colloidal quantum-dots and dye-sensitized metal oxide devices have been demonstrated as next generation photovoltaic materials.[1–4] However, the emerging hybrid organic–inorganic perovskite materials based on lead halides have attracted substantial attention due to their outstanding physical properties such as high absorption coefficients, excellent carrier transports with long electron–hole diffusion lengths, low exciton binding energies and easily tunable energy band gaps;[5–7] these remarkable physical characteristics have led to high power conversion efficiencies (PCE) since the first research in the area of solution-processed perovskite solar cells (PeSCs) was reported in 2009.[8] To achieve highly efficient PeSCs, the perovskite layer must be deposited with a uniform, highly crystalline and dense morphology, and it must completely cover the underlying surface. Diverse methods such as vapor-assisted deposition, solvent engineering and intermolecular exchange have been introduced to produce uniform perovskite films with large crystal domains and complete surface coverage.[9–11] Diverse approaches to improve device performance *via* control of the film morphology have been introduced, and they include interface engineering, induced crystallization with non-solvents, incorporation of processing additives, and nuclei growth.[12–15] In the case of interfacial engineering, suitable interfacial condition for charge transport is obtained, and the energy band structure is tuned *via* doping; it is still one of the most widely employed techniques.[16–20] Recently, Nho *et al.* reported that addition of metal carbonate led to the improvement in the electron extracting properties of a zinc oxide (ZnO) layer *via* modification of its energy levels;[21] this result suggests that metal carbonates may be applied to improve the device performance if the energy level of the doped electron transport layer (ETL) matches with the conduction band of the perovskite active layer. In this regard, ZnO nanoparticles (NPs) have been used as an ETL in our study due to their outstanding electrical and optical properties as well as easily controlled doping, morphology and composition compared to those of conventional TiO_2 ETLs.[22] ZnO NP films may be coated without any thermal treatment and additionally, ZnO possesses a higher conductivity than TiO_2, which may facilitate electron transport.[23] Despite these advantages, to date, the highest device efficiency using ZnO ETLs has only reached 17.1% compared to that of TiO_2-based ETLs, which have achieved over 20% PCE; this suggests that the performance of ZnO-based devices can be further improved considerably.[11,24] Although most of the efficient perovskite solar cell devices reported to date have utilized methylammonium lead iodide ($MAPbI_3$) as an active layer material, formamidinium lead iodide has also been

[a]*Perovtronics Research Center, Department of Energy Engineering, Ulsan National Institute of Science and Technology (UNIST), Ulsan 44919, South Korea. E-mail: jykim@unist.ac.kr*

[b]*Department of Physics, Ulsan National Institute of Science and Technology (UNIST), Ulsan 44919, South Korea*

[c]*Department of Chemistry, Kyung Hee University, Seoul 02447, Republic of Korea*

† Electronic supplementary information (ESI) available. See DOI: 10.1039/c8ra02637h

‡ These authors contributed equally.

demonstrated to yield high-efficiency devices. One promising approach to improve the performance of ZnO ETL-based devices is using $FAPbI_3$ as opposed to $MAPbI_3$ as an active layer material. $FAPbI_3$ has several key advantages including a lower band gap, which is closer to the Shockley–Queisser optimum, improved stability and weaker hysteresis due to well-balanced electron and hole transport compared to $MAPbI_3$.[25] Additionally, FA cations offer the potential for improved chemical compatibility and stability compared to MA cations. Despite the advantages of ZnO compared to those of TiO_2, ZnO thin films have compatibility problems when they are in contact with $MAPbI_3$. For example, Yang *et al.* reported that the ZnO layer reacted with $MAPbI_3$ in an acid–base reaction upon annealing the devices.[26] Since ZnO has a natural basic characteristic, it is able to deprotonate the methylammonium cation and hence degrade the $MAPbI_3$ layer into methylamine and PbI_2 at elevated temperatures. To overcome this issue, Song *et al.* reported that $FAPbI_3$ active layers possessed greater thermal and chemical stability in ZnO ETL devices due to the difficulty of deprotonating the resonance-stabilized FA cations.[27] Despite the potential of this architecture, very few researchers have investigated the utilization of $FAPbI_3$ active layers in conjunction with ZnO ETLs. Previously reported studies indicate that metal carbonate materials lead to improved electron extraction through modification of the electron transport properties and energy level of the ZnO layer. In this study, we have investigated the use of alkali metal carbonates in conjunction with ZnO ETLs to improve the performance of this type of device. Herein, we demonstrate n-i-p-type planar heterojunction perovskite solar cells employing spin-coated ZnO nanoparticles modified with various alkali metal carbonates including Li_2CO_3, Na_2CO_3, K_2CO_3 and Cs_2CO_3, which can tune the energy band structure of ZnO ETLs. Since these metal carbonates doped on ZnO ETLs lead to deeper conduction bands in ZnO ETLs, the electrons are easily transported from the perovskite active layer to the cathode electrode. PCEs can be improved from 11% to 14% *via* incorporation of alkali carbonates in ETLs.

2. Experimental

2.1 Materials and characterization

Preparation of ZnO nanoparticles. ZnO nanoparticles were prepared by the reaction between a zinc acetate solution (23.6 mg ml^{-1} [$Zn(CH_3COO)_2 \cdot 2H_2O$] in methanol) and a potassium hydroxide solution (31.6 mg ml^{-1} in methanol in a 250 ml round bottom flask at 60 °C for 21 h with stirring).[28] Then, these particles were dissolved in a CF : methanol mixture.

Preparation of the perovskite precursor. MAI was prepared by reacting 30 ml of methylamine solution (40% in water) with 30 ml of hydroiodic acid (57 wt% in water) in a 250 ml round bottom flask at 0 °C for 2 h with stirring in an argon environment. The solvent was thermally evaporated under vacuum at 60 °C for 1 h to obtain a white crude product, which was washed with diethyl ether three times. After filtration, the product was dissolved in ethanol and recrystallized for 20 h using ethanol. The precipitate was then washed with diethyl ether and filtered, and the filtered solid was dried at 60 °C under vacuum for 24 h. FAI was prepared by reacting 0.45 g ml^{-1} solution of formamidinium acetate in absolute methanol with 30 ml of HI. The reaction conditions and cleaning process were the same as those for the MAI preparation. To prepare the perovskite precursors, first, PbI_2 was dissolved in DMF (1.3 M) with NMP (1 mM) and second, FAI (or MAI) was dissolved in isopropanol having concentration of 80 mg ml^{-1} (65 mg ml^{-1} for MAI). The obtained solution was stirred at room temperature for 1 h in air and used subsequently for device fabrication.

2.2 Solar cell fabrication and characterization

ITO-coated glass substrates were washed by ultrasonication with DI water, acetone, and isopropanol for 20 minutes each. ZnO nanoparticles were spin-coated at 3000 rpm for 10 s. For the perovskite layer, PbI_2 was dissolved in DMF and spin-coated at 5000 rpm for 30 s. Second, 80 mg ml^{-1} FAI in isopropanol was dropped on the PbI_2 film, spin-coated at 5000 rpm for 30 s and dried at 130 °C for 20 min. The procedure for MAI was similar to that of FAI apart from the concentration and annealing conditions, which were 65 mg ml^{-1} and 100 °C for 2 min, respectively. During this process, the perovskite film was formed. Twenty mg ml^{-1} P3HT dissolved in CB was deposited on the perovskite layer by spin coating at 1000 rpm for 30 s. In this case, P3HT solution did not contain any dopants such as Li-TFSI or TBP. Finally, 70 nm gold was deposited by thermal evaporation under vacuum (<10^{-6} Torr). The current density–voltage (*J*–*V*) characterization of the solar cell devices was obtained using a Keithley 2635A Source Measure Unit under AM1.5G with an irradiation intensity of 100 mW cm^{-1}. The active layer was 0.13 cm^2. External Quantum Efficiency (EQE) measurements were obtained with the PV measurement QE system under ambient conditions, with monochromated light from a xenon arc lamp. Scanning electron microscope measurements (SEM) were obtained using an S-4800 Hitachi high-Technology microscope. SEM samples were prepared by depositing perovskite precursor solutions on ZnO or doped ZnO layers by a spin-coating two-step method, followed by annealing at 130 °C for 10 min on a hotplate. UV-vis absorption was measured using a Varian Cary 5000 spectrophotometer. AFM images were obtained using a Veeco Multimode AFM microscope in a tapping mode.

3. Results and discussion

3.1 Thermal stability and device performance of FAI-based perovskite solar cells

To characterize the relative stabilities of $MAPbI_3$ and $FAPbI_3$ perovskite layers on ZnO films, we deposited perovskite layers on ZnO substrates and heated them for variable amounts of time. MAI and FAI solutions were dripped onto the PbI_2 substrates that were already deposited by spin coating and then, we spin-coated them to form perovskite layers in a nitrogen atmosphere. Detailed fabrication procedures are included in the experimental section. To study the perovskite film construction with ZnO and ZnO with alkali metal carbonate Cs_2CO_3 substrate, X-ray diffraction (XRD) was conducted, as shown in Fig. S1.†

The perovskite XRD peak positions of ZnO and ZnO with Cs_2CO_3 substrate were identical. These results indicated that ZnO with the alkali metal carbonate can be a good substrate for perovskite films.[29] The thermal stabilities were also tested, and the corresponding visual images of the $MAPbI_3$ and $FAPbI_3$ films are shown in Fig. S2(a).† After 30 min at 100 °C, the $MAPbI_3$ film began to decompose and after 90 min, the film was completely decomposed to MAI and PbI_2 at the edges, as indicated by a yellow color.[27] However, the $FAPbI_3$ film was very stable after 120 min at 100 °C. To study the operating stability of the $FAPbI_3$ device, the steady state stability of $FAPbI_3$ on ZnO substrate was tested for 600 s at room temperature under the illumination conditions, as shown in Fig. S2(b).† The device performance did not critically change under the operating conditions, which indicated that the $FAPbI_3$ film had not transformed to other phases at elevated temperatures and under the operating conditions of the device.

The decomposition region gradually increased over 90 min until the entire $MAPbI_3$ film changed from dark brown to yellow. In contrast, after 120 min, the $FAPbI_3$ film did not exhibit any visible decomposition, and the color remained dark without any change, confirming that $FAPbI_3$ has better thermal stability with ZnO than $MAPbI_3$. We prepared solar cell devices based on both $MAPbI_3$ and $FAPbI_3$ to compare their characteristics. Relatively less information is available about optimal processing conditions for depositing $FAPbI_3$ films on ZnO substrates, and the formation of a uniform $FAPbI_3$ film is difficult due to the large cation size of FA^+.[30] Therefore, we optimized the processing conditions for each perovskite layer on ZnO. Fig. 1a shows a schematic diagram of the device architecture used in this study, which comprises sequentially deposited ZnO/perovskite/poly(3-hexylthiophene-2,5-diyl) (P3HT)/Au on indium tin oxide (ITO) substrates. In Fig. 1b, the cross-sectional scanning electron microscopy (SEM) image shows complete device stack, revealing that the perovskite materials fully cover the ZnO layer without any defects. Fig. 2a shows the current density–voltage characteristics of $MAPbI_3$ compared to those of $FAPbI_3$ under simulated solar irradiation. The $MAPbI_3$ solar cell exhibited a lower short circuit current density (J_{SC}) of 18.9 mA cm^{-2}, higher open circuit voltage (V_{OC}) of 1.02 V, and fill factor (FF) of 0.55, with an overall power conversion efficiency (PCE) of 10.7%. The $FAPbI_3$ solar cell exhibited higher J_{SC} of 21.2 mA cm^{-2}, smaller V_{OC} of 0.96 V, FF of 0.58 and PCE of 11.7% (Table 1). $FAPbI_3$ exhibited a bandgap that was closer to the Shockley–Queisser maximum at 1.40 eV; thus, even though V_{OC} was smaller relative to that of $MAPbI_3$, the increased absorption and J_{SC} caused an overall increase in the maximum possible efficiency, which was reflected in our data. Fig. 2b shows the incident photon to charge carrier efficiency (IPCE) spectra, revealing a photocurrent onset near 870 nm in the case of $FAPbI_3$, which was notably higher than that of $MAPbI_3$ (~800 nm). The device results, in addition to thermal stability results, indicated that $FAPbI_3$ is a preferable active layer material for use in conjunction with ZnO ETLs, and the remainder of our study focuses on devices based on this material.

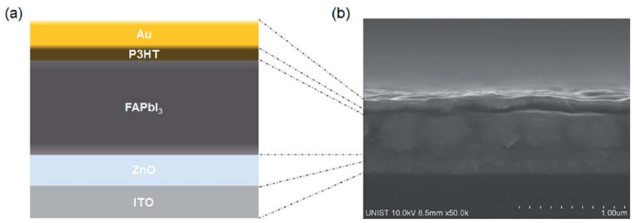

Fig. 1 (a) Schematic diagram and (b) SEM cross section images of the conventional planar perovskite solar cell with doped ZnO.

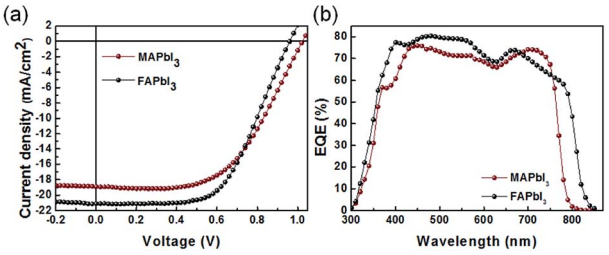

Fig. 2 (a) Current density–voltage characteristics of $MAPbI_3$ and $FAPbI_3$ planar solar cells under 100 mW cm^{-2} AM1.5 illumination. (b) External quantum efficiency spectra of each cell.

Table 1 Solar cell characteristics of each $MAPbI_3$ and $FAPbI_3$ device

	J_{SC} (mA cm^{-2})	V_{OC} (V)	FF	PCE (%)	Cal. J_{SC} (mA cm^{-2})
$MAPbI_3$	18.9	1.02	0.55	10.7	17.5
$FAPbI_3$	21.1	0.96	0.58	11.7	19.7

3.2 Energy band characterization

To further improve the device performance, we sought to modify ZnO ETLs with alkali metal carbonates.[21] We found that the energy band structure of the spin-coated ZnO nanoparticles could be modified with various alkali metal carbonates including Li_2CO_3, Na_2CO_3, K_2CO_3, and Cs_2CO_3. Since these metal carbonates doped on ZnO ETLs lead to deeper conduction bands in the ZnO ETLs, electron transport from the perovskite active layer to the cathode electrode was easy due to low energy barrier.

To investigate the influence of alkali metal carbonates on the electrical properties of ZnO NP layers, we obtained ultraviolet photoelectron spectra (UPS) and X-ray photoelectron spectra (XPS). XPS plots showing Li 2p, Na 1s, K 2p and Cs 3d regions of the photoelectron spectra are reported in Fig. S3.† Pristine ZnO films did not show any photoemission corresponding to alkali metals; however, clear peaks corresponding to Li 2p, Na 1s, K 2p and Cs 3d emissions were observed for the ZnO films doped with Li_2CO_3, Na_2CO_3, K_2CO_3 and Cs_2CO_3, respectively, confirming that all alkali metals were incorporated into the ZnO NP layers.

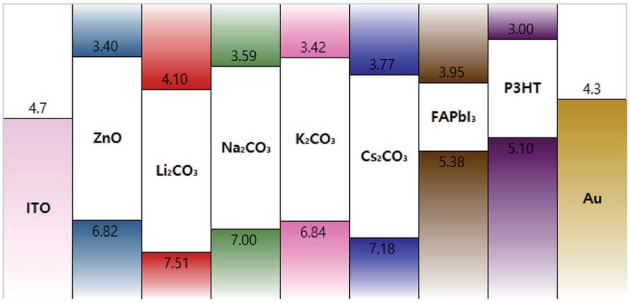

Fig. 3 Energy band diagram of ZnO doped with various alkali metal carbonate materials.

We also observed *via* UPS analysis that the metal carbonates played a substantial role in influencing the energy band structure of ZnO (Fig. S4 and Table S1†). Work functions were calculated from the secondary cut-off edge, whereas the valence band maximum (VBM) of each layer was obtained from the Fermi edge relative to that of a gold reference sample. VBM of pristine ZnO (6.82 eV) was much lower than those of the other samples, whereas ZnO doped with Li_2CO_3 exhibited the deepest VBM of 7.19 eV. Other VB levels included 7.00 eV for Na_2CO_3, 6.84 eV for K_2CO_3, and 7.18 eV for Cs_2CO_3. To calculate the conduction band minima (CBM), we subtracted the observed optical band gaps taken from the Tauc plots (Fig. S5 and Table S2†) from the VBMs measured by UPS. The optical band gaps of pristine ZnO and all of the doped ZnO films were found to be almost identical, and the tendency of the CBM data was similar to the trends observed in the VBM data. As shown in Fig. 3, CBM of pristine ZnO at 3.40 eV was the highest among all the values. Compared to the CBM and VBM levels of pristine ZnO, the CBM and VBM levels of ZnO doped with Cs_2CO_3 and Li_2CO_3 showed the greatest changes. Upon doping with Cs_2CO_3 and Li_2CO_3, the CBM energies dropped to 3.77 eV and 4.10 eV, respectively. Moreover, there was an energy barrier for the extraction of electrons from the CBM of $FAPbI_3$ (3.95 eV) compared to that of pristine ZnO; this barrier was reduced or eliminated after doping with Cs_2CO_3 and Li_2CO_3, and this indicated that electrons can be more easily collected for ZnO ETLs doped with these salts.[31]

3.3 Morphology characterization

To investigate the effect of doping with metal carbonates on the physical structure of the ZnO films, atomic force microscopy (AFM) images and scanning electron microscopy (SEM) images were collected; these images are shown in Fig. S6 and S7,† respectively. AFM images of pristine ZnO and metal carbonate-doped ZnO indicated that the metal carbonates did not drastically affect the film morphology. RMS values were found to be 2.84 nm for ZnO doped with Li_2CO_3, 2.81 nm for ZnO with Na_2CO_3, 3.05 nm for ZnO with K_2CO_3, and 2.48 nm for ZnO with Cs_2CO_3, indicating that the film roughness did not change significantly with metal carbonate doping. The SEM images confirmed that the film morphologies were not dramatically affected by the metal carbonates.

3.4 Electrochemical characterization

To further understand the influence of alkali metal carbonates on the electrical and interfacial properties of solar cell devices, we prepared devices with the architecture ITO/ZnO/M_2CO_3/$FAPbI_3$/P3HT/Au and obtained electrochemical impedance spectra (EIS), as shown in Fig. S8.† EIS provides detailed information about the interfacial properties including the charge carrier recombination rates and electron transport properties to be quantified. Nyquist plots of the devices measured under dark conditions at 0 V are shown in Fig. S8.† All plots exhibited one semicircle without a transmission line (TL). The absence of TL patterns indicated that the recombination of the solar cell may be interpreted by the Gerischer impedance model.[32] Furthermore, the single semicircle indicated that the interface contact between the perovskite layer and the ZnO layer is not likely to be a rectifying contact. In these plots, the diameter of the semicircle is related to the recombination resistance. Notably, the devices using ZnO doped with Cs_2CO_3 or Li_2CO_3 exhibited higher recombination resistances than those with pristine ZnO, whereas the one with K_2CO_3 showed lower recombination resistance. Interestingly, these trends in the recombination resistance showed a strong correlation with both the CBM data obtained by UPS and solar cell device data; this was consistent with a reduced energy barrier for electron extraction, leading to reduced carrier recombination and improved device performance.[21]

3.5 Photovoltaic characterization

Solar cell devices were fabricated using $FAPbI_3$ active layers deposited on ZnO substrates doped with different alkali metal carbonates; Fig. 4a shows the corresponding current density–voltage data. With pristine ZnO, the devices yielded PCE of 11.7%, J_{SC} of 21.1 mA cm^{-2}, V_{OC} of 0.96 V and FF of 0.58. Li_2CO_3 and Cs_2CO_3, which decreased the CBM of ZnO ETLs and increased the carrier recombination resistance, led to improved device performance; notably, FF and J_{SC} of the two devices, that is, ZnO doped with Li_2CO_3 and with Cs_2CO_3 increased significantly. The device doped with Cs_2CO_3 exhibited J_{SC} of 23.1 mA cm^{-2}, V_{OC} of 0.98 V and FF of 0.62 with an overall PCE of 14.1%. The device doped with Li_2CO_3 yielded J_{SC} of 21.7 mA cm^{-2}, V_{OC} of 0.93 V, FF of 0.65 and PCE of 13.0%. Other details related to the performance of each cell are listed in Table 2. As shown in Fig. S7,† this result was obtained due to the uniform and large grain size of the perovskite photoactive layer on the doped ZnO layer, which increased the charge collection efficiency and reduced the recombination.[33,34] To confirm the effect of metal carbonate-doped ZnO, a field-effect transistor (FET) was used to measure the intrinsic mobilities of ZnO and doped ZnO, as shown in Fig. S9(a) and Table S3.† The FET results showed that the electron mobilities of all ZnO materials doped with alkali metal carbonates were higher than that of pristine ZnO by about $\sim 10^{-3}$ to $\sim 10^{-4}$ cm^2 V^{-1} s^{-1}. Furthermore, as compared to the photoluminescences of pristine ZnO and Cs_2CO_3-doped ZnO with perovskite layer, the photoluminescence was dramatically quenched, which directly indicated that the perovskite with ZnO doped with Cs_2CO_3 has efficient charge transfer.

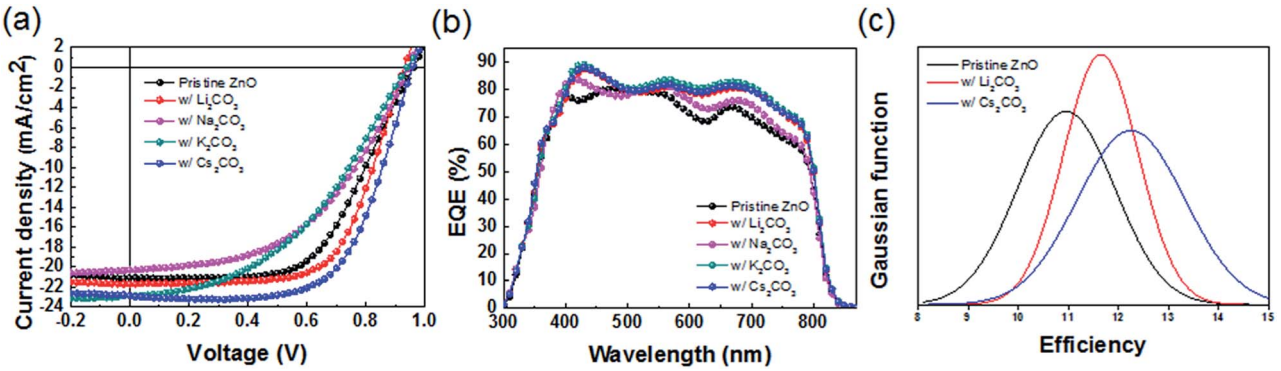

Fig. 4 (a) Current density–voltage characteristics of $FAPbI_3$ planar solar cells deposited on the pristine ZnO layer and each ZnO doped with metal carbonate under 100 mW cm^{-2} AM1.5 illumination. (b) External quantum efficiency spectra of each cell. (c) Gaussian curves of the device efficiency of $FAPbI_3$ perovskite solar cell deposited on the pristine ZnO, ZnO doped with Li_2CO_3, and ZnO doped with Cs_2CO_3.

Table 2 Solar cell characteristics of each $MAPbI_3$ and $FAPbI_3$ device

	J_{SC} (mA cm^{-2})	V_{OC} (V)	FF	PCE (%)	Cal. J_{SC} (mA cm^{-2})
Pristine ZnO	21.1	0.96	0.58	11.7	19.7
w/Li_2CO_3	21.7	0.93	0.65	13.0	21.4
w/Na_2CO_3	20.3	0.94	0.49	9.43	20.3
w/K_2CO_3	22.8	0.94	0.44	9.45	21.9
w/Cs_2CO_3	23.1	0.98	0.62	14.1	21.8

(Fig. S9(b)†) These mobilities and charge transfer properties of alkali metal carbonate-doped ZnO can contribute to improved device performance.

Notably, the trends in efficiency are similar with the trends in recombination resistance and CBM energies. Fig. 4b shows the IPCE curve. The spectral shapes of the devices using ZnO doped with alkali metal carbonates are slightly different than those with pristine ZnO, showing slightly enhanced photocurrent generation in the near-infrared region of the spectrum. Fig. 4c shows PCE statistics for solar cells using $FAPbI_3$ layers deposited on pristine ZnO, ZnO doped with Li_2CO_3 and ZnO doped with Cs_2CO_3, whereas the statistics for individual device parameters are reported in Fig. S10.† This curve shows that devices using ZnO doped with Cs_2CO_3 yielded significantly higher J_{SC} compared to other devices that used pristine ZnO or ZnO doped with Li_2CO_3. To clearly show the significance of the trends in the device data, we analysed the characteristics of 50 individual devices to prepare histograms of J_{SC}, V_{OC}, FF and PCE for $FAPbI_3$ for devices using pristine ZnO and ZnO with alkali carbonate series (Fig. S10†). As shown in Fig. S10a,† the average J_{SC} value of Cs-doped devices significantly increased compared to that of pristine ZnO; the FF values increased for both Li- and Cs-doped devices, whereas the V_{OC} values remained similar (Fig. S10b†) for all conditions. Fig. S10d† shows that the average efficiency of the devices followed the same trend as that of J_{SC}, and PCEs improved from 11% to 14% *via* incorporation of alkali carbonates in ETLs.

4. Conclusions

In summary, we successfully investigated high performance $FAPbI_3$ perovskite solar cells using doped alkali carbonates including Li_2CO_3, Na_2CO_3, K_2CO_3 and Cs_2CO_3 on ZnO ETLs using low temperature solution processing techniques. This report is one of the first studies to utilize a formamidinium-based active layer in conjunction with ZnO ETLs. We found that alkali carbonates could modify the CB level of the ZnO electron transport layer, leading to improved electron transport and extraction compared to un-doped ZnO ETLs. As a result, the perovskite solar cell using Cs-doped ZnO showed higher performance than those using other alkali metal carbonates with over 14.1% PCE. As alternatives to TiO_2 and n-type metal oxides, doped ZnO nanoparticle electron transport materials constitute viable ETLs for efficient n-i-p planar heterojunction solar cells, which can be used on flexible substrates *via* roll-to-roll processing.

Conflicts of interest

There are no conflicts of interest to declare.

Acknowledgements

This work was supported by the National Research Foundation of Korea Grant (NRF) (2016R1C1B2016188, 2017R1A2B3010049). This research was also funded by the Ulsan National Institute of Science and Technology (UNIST) (1.170003.01).

Notes and references

1 B. O'Regan and M. Gratzel, *Nature*, 1991, **353**, 737–740.
2 S. H. Im, H.-j. Kim, S. W. Kim, S.-W. Kim and S. I. Seok, *Energy Environ. Sci.*, 2011, **4**, 4181–4186.
3 G. Li, R. Zhu and Y. Yang, *Nat. Photonics*, 2012, **6**, 153–161.
4 G.-H. Kim, B. Walker, H.-B. Kim, J. Y. Kim, E. H. Sargent, J. Park and J. Y. Kim, *Adv. Mater.*, 2014, **26**, 3321–3327.

5 M. M. Lee, J. Teuscher, T. Miyasaka, T. N. Murakami and H. J. Snaith, *Science*, 2012, **338**, 643–647.
6 S. D. Stranks, G. E. Eperon, G. Grancini, C. Menelaou, M. J. P. Alcocer, T. Leijtens, L. M. Herz, A. Petrozza and H. J. Snaith, *Science*, 2013, **342**, 341–344.
7 G. Xing, N. Mathews, S. Sun, S. S. Lim, Y. M. Lam, M. Grätzel, S. Mhaisalkar and T. C. Sum, *Science*, 2013, **342**, 344–347.
8 A. Kojima, K. Teshima, Y. Shirai and T. Miyasaka, *J. Am. Chem. Soc.*, 2009, **131**, 6050–6051.
9 Q. Chen, H. Zhou, Z. Hong, S. Luo, H.-S. Duan, H.-H. Wang, Y. Liu, G. Li and Y. Yang, *J. Am. Chem. Soc.*, 2014, **136**, 622–625.
10 N. J. Jeon, J. H. Noh, Y. C. Kim, W. S. Yang, S. Ryu and S. I. Seok, *Nat. Mater.*, 2014, **13**, 897–903.
11 W. S. Yang, J. H. Noh, N. J. Jeon, Y. C. Kim, S. Ryu, J. Seo and S. I. Seok, *Science*, 2015, **348**, 1234–1237.
12 J. Peet, J. Y. Kim, N. E. Coates, W. L. Ma, D. Moses, A. J. Heeger and G. C. Bazan, *Nat. Mater.*, 2007, **6**, 497–500.
13 J. K. Lee, W. L. Ma, C. J. Brabec, J. Yuen, J. S. Moon, J. Y. Kim, K. Lee, G. C. Bazan and A. J. Heeger, *J. Am. Chem. Soc.*, 2008, **130**, 3619–3623.
14 W. Chen, M. P. Nikiforov and S. B. Darling, *Energy Environ. Sci.*, 2012, **5**, 8045–8074.
15 S. Song, M. T. Horantner, K. Choi, H. J. Snaith and T. Park, *J. Mater. Chem. A*, 2017, **5**, 3812–3818.
16 J. H. Seo, A. Gutacker, Y. Sun, H. Wu, F. Huang, Y. Cao, U. Scherf, A. J. Heeger and G. C. Bazan, *J. Am. Chem. Soc.*, 2011, **133**, 8416–8419.
17 S. Y. Park, B. J. Kim, K. Kim, M. S. Kang, K.-H. Lim, T. I. Lee, J. M. Myoung, H. K. Baik, J. H. Cho and Y. S. Kim, *Adv. Mater.*, 2012, **24**, 834–838.
18 B. R. Lee, E. D. Jung, Y. S. Nam, M. Jung, J. S. Park, S. Lee, H. Choi, S.-J. Ko, N. R. Shin, Y.-K. Kim, S. O. Kim, J. Y. Kim, H.-J. Shin, S. Cho and M. H. Song, *Adv. Mater.*, 2014, **26**, 494–500.
19 S. Kwon, K.-G. Lim, M. Shim, H. C. Moon, J. Park, G. Jeon, J. Shin, K. Cho, T.-W. Lee and J. K. Kim, *J. Mater. Chem. A*, 2013, **1**, 11802–11808.
20 H. Choi, J. S. Park, E. Jeong, G.-H. Kim, B. R. Lee, S. O. Kim, M. H. Song, H. Y. Woo and J. Y. Kim, *Adv. Mater.*, 2011, **23**, 2759–2763.
21 S. Nho, G. Baek, S. Park, B. R. Lee, M. J. Cha, D. C. Lim, J. H. Seo, S.-H. Oh, M. H. Song and S. Cho, *Energy Environ. Sci.*, 2016, **9**, 240–246.
22 D. Liu and T. L. Kelly, *Nat. Photonics*, 2014, **8**, 133–138.
23 K. Mahmood, S. B. Park and H. J. Sung, *J. Mater. Chem. C*, 2013, **1**, 3138–3149.
24 M. Saliba, T. Matsui, J.-Y. Seo, K. Domanski, J.-P. Correa-Baena, M. K. Nazeeruddin, S. M. Zakeeruddin, W. Tress, A. Abate, A. Hagfeldt and M. Gratzel, *Energy Environ. Sci.*, 2016, **9**, 1989–1997.
25 N. J. Jeon, J. H. Noh, W. S. Yang, Y. C. Kim, S. Ryu, J. Seo and S. I. Seok, *Nature*, 2015, **517**, 476.
26 J. Yang, B. D. Siempelkamp, E. Mosconi, F. De Angelis and T. L. Kelly, *Chem. Mater.*, 2015, **27**, 4229–4236.
27 J. Song, W. Hu, X.-F. Wang, G. Chen, W. Tian and T. Miyasaka, *J. Mater. Chem. A*, 2016, **4**, 8435–8443.
28 P. R. Brown, R. R. Lunt, N. Zhao, T. P. Osedach, D. D. Wanger, L.-Y. Chang, M. G. Bawendi and V. Bulović, *Nano Lett.*, 2011, **11**, 2955–2961.
29 F. Ma, J. Li, W. Li, N. Lin, L. Wang and J. Qiao, *Chem. Sci.*, 2017, **8**, 800–805.
30 G. E. Eperon, S. D. Stranks, C. Menelaou, M. B. Johnston, L. M. Herz and H. J. Snaith, *Energy Environ. Sci.*, 2014, **7**, 982–988.
31 S. Song, G. Kang, L. Pyeon, C. Lim, G.-Y. Lee, T. Park and J. Choi, *ACS Energy Lett.*, 2017, **2**, 2667–2673.
32 V. Gonzalez-Pedro, E. J. Juarez-Perez, W.-S. Arsyad, E. M. Barea, F. Fabregat-Santiago, I. Mora-Sero and J. Bisquert, *Nano Lett.*, 2014, **14**, 888–893.
33 J. Jeong, H.-B. Kim, H. Kim, B. Walker, S. Song, J. Heo, Y. J. Yoon, Y. Jo, H. Choi, G.-H. Kim, D. S. Kim and J. Y. Kim, *ACS Energy Lett.*, 2016, **1**, 712–718.
34 A. S. Zoolfakar, R. A. Rani, A. J. Morfa, S. Balendhran, A. P. O'Mullane, S. Zhuiykov and K. Kalantar-zadeh, *J. Mater. Chem.*, 2012, **22**, 21767–21775.